A quantum spin liquid based on a new three-dimensional lattice

S. Chillal[1,*], Y. Iqbal[2], H. O. Jeschke[3], J. A. Rodriguez-Rivera[4,5], R. Bewley[6], P. Manuel[6], D. Khalyavin[6], P. Steffens[7], R. Thomale[8], A. T. M. N. Islam[1], J. Reuther[1,9], and B. Lake[1,10]

[1]Helmholtz-Zentrum Berlin für Materialien und Energie, Hahn-Meitner Platz 1, 14109 Berlin, Germany

[2]Department of Physics, Indian Institute of Technology Madras, Chennai 600036, India

[3]Research Institute for Interdisciplinary Science, Okayama University, 3-1-1 Tsushima-naka, Kita-ku, Okayama 700-8530, Japan

[4]NIST Center for Neutron Research, National Institute of Standards and Technology, 20899 Gaithersburg, USA

[5]Department of Materials Science, University of Maryland, College Park, 20742 Maryland, USA

[6]ISIS Facility, STFC Rutherford Appleton Laboratory, Oxfordshire OX11 0QX, UK

[7]Institut Laue-Langevin, 71 Avenue des Martyrs, 38042 Grenoble Cedex 9, France

[8]Institute for Theoretical Physics and Astrophysics, Julius-Maximilian's University of Würzburg, Am Hubland, D-97074 Würzburg, Germany

[9]Dahlem Center for Complex Quantum Systems and Fachbereich Physik, Freie Universität Berlin, 14195 Berlin, Germany

[10]Institut für Festkörperphysik, Technische Universität Berlin, Hardenbergstr. 36, 10623 Berlin, Germany

[*]Correspondence: shravani.chillal@helmholtz-berlin.de

December 22, 2017

The quantum spin liquid is a highly entangled magnetic state characterized by the absence of long-range magnetic order or any static magnetism in its ground state. Instead the spins are continuously fluctuating in a highly correlated way down to the lowest temperatures. The spin liquid state is very rare and is confined to a few specific cases where the interactions between the magnetic ions cannot be simultaneously satisfied (known as frustration). In particular, lattices with magnetic ions in triangular or tetrahedral arrangements which interact via isotropic antiferromagnetic interactions can generate frustration because it is impossible to connect all the bonds with magnetic moments that are aligned antiparallel. This leads to highly degenerate ground states between which the magnetic moments fluctuate continuously. Three-dimensional isotropic spin liquids have mostly been sought in materials where the magnetic ions form pyrochlore or hyperkagome lattices. Here we discover a new type of three-dimensional lattice that enables spin liquid behavior called the hyper-hyperkagome lattice which manifests in the compound $PbCuTe_2O_6$. Using a combination of experiment and theory we show that this system satisfies all the requirements for a quantum spin liquid including the absence of static magnetism, the presence of a degenerate manifold of ground states, and the characteristic continuum of spinon excitations. This result is important because, it points to new ways to engineer spin liquid behavior.

The excitations of a quantum spin liquid are called spinons, which cannot be excited individually by any experimental technique but are instead created in pairs in contrast to the conventional spin-wave excitations which are usually created singly [1]. As a consequence, these excitations are observed as a broad multi-spinon continuum in contrast to spin-waves which appear as sharp modes. Spinons possess fractional quantum numbers such as those of one-dimensional antiferromagnets formed from half-integer spin magnetic ions, which have quantum spin number $S=\frac{1}{2}$ and can only be created in multiple pairs [2, 3, 4]. In two-dimensions, the best known spin liquid model is the kagome lattice which consists of antiferromagnetically-coupled, corner-sharing triangles, as realized in the mineral Herbertsmithite ($ZnCu_3(OH)_6Cl_2$) [5], while a more complex kagome bilayer Hamiltonian realized by $Ca_{10}Cr_7O_{28}$ was also found to support spin liquid behaviour [6, 7]. The excitations of both these compounds were observed by inelastic neutron scattering to form diffuse dispersionless rings suggestive of multi-spinon continua, in striking contrast to sharp and dispersive spin-wave modes. Diffuse features were also observed in the two-dimensional honeycomb magnet α-$RuCl_3$ which lies close to the Kitaev spin liquid state due to competition between interactions with mutually perpendicular anisotropies [8, 9].

Frustration can also be achieved by three-dimensional arrangements of triangles or tetrahedra. The pyrochlore lattice which consists of a three-dimensional network of corner-sharing tetrahedra can support

a number of spin liquid states [10, 11, 12, 13, 14]. In the case of isotropic interactions, a Heisenberg spin liquid is predicted, as is realized by $Lu_2Mo_2O_5N_2$ [15], while for magnetic ions with local Ising anisotropy the spin ice state is expected [16] as realised by $Dy_2Ti_2O_7$ and $Ho_2Ti_2O_7$ [17, 18]. As for two-dimensional spin liquids, the excitations are observed as a broad diffuse pattern of multi-particle features in inelastic neutron scattering. In contrast to the advanced exploration of the pyrochlore spin liquids, current understanding of three-dimensional networks of corner-sharing triangles as exemplified by the hyperkagome lattice is much less developed, although this is also expected to support spin liquid behavior in the presence of antiferromagnetic interactions [19, 20, 21]. There are two physical realizations of the hyperkagome, namely, $Gd_3Ga_5O_{12}$ and $Na_4Ir_3O_8$, both of which show proximity to spin liquid states, although at lowest temperatures $Na_4Ir_3O_8$ develops a static spin glass ground state [22] while $Gd_3Ga_5O_{12}$ develops long-range magnetic order due to anisotropy and additional terms in the Hamiltonian [23].

In this article, we explore a new three-dimensional magnet consisting of antiferromagnetically coupled $S=\frac{1}{2}$ ions which form a three-dimensional network of corner-sharing triangles related to but distinctly different from the hyperkagome lattice. By performing a combined experimental and theoretical investigation we develop a consistent picture of its ground state that does not develop any static magnetism, and its excitations which form diffuse and dispersionless spheres suggesting spinon excitations. Together, these results point to a quantum spin liquid based on a new type of lattice.

The compound $PbCuTe_2O_6$ contains Cu^{2+} ions which have spin-$\frac{1}{2}$ magnetic moments. Synthesis and measurements of powder samples of this compound have been previously reported [24, 25]. DC magnetic susceptibility yields a Curie-Weiss temperature of $\theta_{\rm CW} = -22$ K revealing predominantly antiferromagnetic exchange interactions [24]. Although heat capacity shows a broad maximum at 1.15 K and a weak kink at 0.87 K [24], neither feature corresponds to a sharp λ-type anomaly and there is no phase transition to long-range magnetic order. Muon spin resonance measurements confirm the absence of any static magnetism down to 0.02 K [25]. They do however, reveal enhanced magnetic correlations at low temperatures ($T < 1$ K) implying the presence of persistent spin dynamics in the ground state as is typical of a quantum spin liquid.

The positions of the magnetic Cu^{2+} ions in $PbCuTe_2O_6$ are shown in Figure 1a where the green and red bonds represent the $1^{\rm st}$ and $2^{\rm nd}$ nearest neighbour interactions J_1 and J_2, respectively. On its own J_1 couples the Cu^{2+} moments into isolated triangles, while J_2 forms a three-dimensional network of corner-sharing triangles known as the *hyperkagome* lattice. Further neighbour interactions should also be considered and as shown in Figure 1b, the $3^{\rm rd}$ neighbour interaction J_3 forms isolated chains running parallel to the crystalline **a**, **b**, **c** axes and the $4^{\rm th}$ neighbour interaction J_4, is responsible for chains

parallel to the body diagonals. The complete Hamiltonian is

$$\mathcal{H} = \sum_{k=1,2,3,4(i<j)} J_k \mathbf{S}_i \cdot \mathbf{S}_j, \tag{1}$$

where the interactions have been assumed to be isotropic, thus allowing the spins to point in any direction. This is justified because, as a light transition metal ion with only one hole in the $3d$ shell, the orbital moment of Cu^{2+} is quenched by the strong square-planar crystal field due to the surrounding O^{2-} ion. DC susceptibility confirms that the interactions are isotropic, since it is almost independent of the direction of the applied magnetic field [see supplemental material].

In this work we provide strong experimental and theoretical evidence for the quantum spin liquid state in $PbCuTe_2O_6$. We perform neutron diffraction and inelastic neutron scattering measurements and show that the absence of long-range magnetic order in the ground state of this compound is accompanied by diffuse spheres of dispersionless inelastic scattering as expected for a continuum of spinon excitations. We also determine the exchange interactions using density functional theory and establish that a new and unexplored frustrated motif is responsible for this behaviour. Finally, we reproduce the observed ground state and dynamics using pseudo-fermion functional renormalization group calculations and discuss the origins of the spin liquid state in $PbCuTe_2O_6$.

Results

Absence of magnetic ordering

The heat capacity of $PbCuTe_2O_6$ reveals an anomaly at the temperature T_{an}=0.87 K [24]. Although this is clearly not a sharp λ-anomaly and is unlikely to indicate a phase transition, further verification of the magnetic ground state is necessary. Neutron diffraction directly measures the spatial Fourier transform of the spin-spin correlation function and would show resolution-limited magnetic Bragg peaks in the case of long-range magnetic order. Figure 2a shows the neutron powder diffraction patterns of $PbCuTe_2O_6$ measured above and below T_{an} at temperatures T= 2 K and 0.1 K, respectively. Both patterns can be described entirely by considering only the known crystal structure of $PbCuTe_2O_6$ [26]. The absence of any additional Bragg peaks that could correspond to long-range magnetic order is further revealed by taking the difference between the diffraction patterns at these two temperatures as shown by the lower green curve. To establish an upper limit on the maximum size of any possible static ordered moment, several magnetic structures were simulated and compared to the data. Figure 2b shows a magnetic Bragg peak compatible with the magnetic structure of the iso-structural compound $SrCuTe_2O_6$. The ordered moment if present must be smaller than $\approx 0.05\mu_B/Cu^{2+}$ which is much less

than the total spin moment of the Cu^{2+} ion of $1\mu_B$ indicating that static magnetism is suppressed.

Spinon-like excitations

To explore the magnetic excitations of $PbCuTe_2O_6$, we performed inelastic neutron scattering. This technique directly measures the dynamical structure factor $S(\mathbf{Q}, E)$, which is the Fourier transform in space and time of the spin-spin correlation function and allows the magnetic excitation spectrum to be mapped out as a function of energy E and momentum (or wavevector) transfer $\mathbf{Q}$. Figure 3a shows the excitation spectrum of a powder sample measured at T= 0.1 K. A dispersionless, broad diffuse band of magnetic signal is clearly visible around momentum transfer $|Q| \approx 0.8$ Å^{-1}. The magnetic excitations extend up to 3 meV and are clearly much broader than the instrumental resolution. To obtain a more detailed picture, inelastic neutron scattering was performed on single crystal samples at several fixed energy transfers. Figure 3b-d show the excitations in the $[h, k, 0]$-plane measured at E=0.75, 1.5 and 2 meV, respectively, while Figure 4b gives the scattering at E=0.5 meV. For all energy transfers, the excitations form a diffuse ring at $|Q| \approx 0.8$ Å^{-1}, while additional weaker branches of scattering extend outwards to higher wavevectors. At low energy transfers ($E < 1$ meV) the diffuse ring has double maxima at wavevectors $(1.69, \sim \pm 0.3, 0)$ and $(\sim \pm 0.3, 1.69, 0)$, etc (see Figure 4h) while at higher energies it broadens and becomes weaker. The ring can also be observed in the $[h, h, l]$-plane where its intensity also modulates (as shown in Figure 4a for E=0.5 meV), together these results indicate that the excitations in fact form a diffuse sphere in reciprocal space with a radius of $|Q| \approx 0.8$ Å^{-1}. The excitations of $PbCuTe_2O_6$ are clearly very different from the sharp and dispersive spin-wave excitations expected in conventional magnets with long-range magnetically order ground states or from the gapped and dispersive magnon excitations of dimer magnets [27, 28]. Diffuse scattering features indicate a multi-spinon continuum of excitations as have been well-documented in one-dimensional antiferromagnets formed from half-integer spin magnetic ions [2, 3, 4]. They have also been observed in several two-dimensional quantum spin liquids where similar diffuse ring-like features have been found [5, 6]. In three-dimensions, most spin liquid candidates are based on the pyrochlore structure and the spinon excitations form a distinctive pinch-point pattern [29].

Magnetic Hamiltonian

Having confirmed that $PbCuTe_2O_6$ exhibits the characteristic features of a quantum spin liquid, we now investigate the origins of this behaviour by deriving the exchange interactions. For this purpose, we employ density functional theory (DFT). The resulting values of the interaction strengths are plotted as a function of the onsite interaction "U" in Figure 1c for U=5.5 eV to 8 eV as this range spans the usual

values for the Cu^{2+} onsite correlation strength. We find that all the interactions are antiferromagnetic. In contrast to previous DFT calculations where the hyperkagome interaction J_2 was found to be much stronger than the other interactions [24], we find that the two frustrated interactions J_1 and J_2 are of almost equal strength and are significantly stronger than the chain interactions J_3 and J_4. The combined effect of J_1 and J_2 is to couple the Cu^{2+} ions into a highly frustrated three-dimensional network of corner-sharing triangles similar to the hyperkagome lattice (J_2 only) but with a higher density of triangles. In the hyperkagome lattice each magnetic ion participates in two corner-sharing triangles, while in $PbCuTe_2O_6$ each Cu^{2+} ion participates in three triangles resulting in a higher connectivity - we name this lattice the hyper-hyperkagome. As shown in Figure 1c, the values of the exchange interactions decrease as the value of U increases. For each value of U the resulting set of interactions strengths can be used to calculate the Curie-Weiss temperature $\theta_{\rm CW}$. Since DC susceptibility measurements yield $\theta_{\rm CW} = -22$ K [24, 25], we use U=7.5 eV (corresponding to $\theta_{\rm CW} = -23$ K) giving interaction sizes J_1=1.13 meV, J_2=1.07 meV, J_3=0.59 meV, and J_4=0.12 meV.

Comparison to theory

To gain further insight into the quantum spin liquid behavior of $PbCuTe_2O_6$, the static susceptibility expected from this set of interactions was calculated using the theoretical technique of pseudo-fermion functional renormalization group (PFFRG). In agreement with the experimental observations, the susceptibility does not show any sign of long-range magnetic order even down to the lowest temperatures confirming that static magnetism is suppressed by this Hamiltonian. The momentum resolved susceptibility calculated at T=0.2 K is shown in Figure 4c-d for the $[h, k, 0]$- and $[h, h, l]$-planes respectively. It predicts a diffuse sphere of scattering at the same wave-vectors and with similar intensity modulations as those observed experimentally (Figure 3b-d and 4a-b), and even able to reproduce the weaker features. The accuracy of the calculations can be further demonstrated by comparing cuts through the data and simulations. As shown in Figure 4g-h the theory reproduces the double maxima as well as the structure of the slopes of these peaks to high precision. We emphasize that this level of agreement has hardly ever been achieved for a material with many competing interactions on a complicated three-dimensional lattice and in the extreme quantum (spin-1/2) limit. From a more general viewpoint, it demonstrates that the combination of DFT and PFFRG provides a powerful and flexible numerical framework for the investigation of real quantum magnetic materials. The PFFRG method was also used to test the robustness of the spin liquid state to variations in the Hamiltonian. We find that the ground state shows no tendency toward long-range magnetic order when the interactions are varied over $0.975 \leqslant J_1/J_2 \leqslant 1.08$ (corresponding to -37 K $\leqslant \theta_{\rm CW} \leqslant -21$ K) while the susceptibility changes only slightly [Figure 4g-h].

Discussion

The PFFRG calculations confirm that the Hamiltonian of $PbCuTe_2O_6$ supports a quantum spin liquid ground state, however, the question arises as to why this complex Hamiltonian generates such a phase. According to common understanding, a quantum spin liquid can be stabilized when the corresponding classical model exhibits an infinitely large ground-state degeneracy. Even if the classical ground state degeneracy is not extensive to support a spin liquid, quantum fluctuations can often access a larger Hilbert space of energetically nearby states which may prevent the formation of static long-range order. This is the case for $PbCuTe_2O_6$ where PFFRG simulations for the full $J_1{-}J_2{-}J_3{-}J_4$ model show spin liquid behaviour in the quantum limit, while in the classical limit the system develops conventional magnetic order. An interesting explanation for the spin-liquid formation is revealed when only the triangle J_1 and hyperkagome J_2 interactions are considered. In this case, our classical simulations now predict an infinite ground state degeneracy as indicated by the streaks of scattering parallel to the $[1, 1, 1]$ directions shown in Figure 4e. Furthermore, this pattern approximately resembles the PFFRG calculation for quantum spins in the $[h, h, l]$-plane (Figure 4c) although in the quantum case the features are considerably broadened. The discrepancy in the $[h, k, 0]$-plane (compare Figure 4f and d) may be attributed to the fact that the interaction J_3 which creates chains parallel to cubic axes, is strong enough to influence the susceptibility contribution in this plane. The general agreement implies that the relevant fluctuation mechanism that stabilizes the spin liquid phase in $PbCuTe_2O_6$ can be explained by the J_1 and J_2 interactions alone, while the weaker J_3 and J_4 interactions simply modify this phase. The lattice resulting from J_1 and J_2 is a network of corner sharing triangles. In the case of antiferromagnetic interactions, all classical ground states must obey the local constraint that for each triangle, the vector sum of the spins is zero. The large ground-state degeneracy then follows from the fact that there are infinitely many states which fulfill all constraints. This is similar to the spin ice materials, where a local ice rule also gives rise to macroscopic degeneracy. In our case, however, the spin liquid occurs due to a new type of 'ice rule' on a previously unexplored lattice and in the presence of strong quantum fluctuations.

In conclusion, we show using a combination of theory and experiment that $PbCuTe_2O_6$ exhibits all the features expected of a quantum spin liquid including the absence of static magnetism and the presence of diffuse dispersionless spinon-like excitations. Although $PbCuTe_2O_6$ has a complex Hamiltonian it is clear that the frustration arises from the network of corner-sharing triangles due to the dominant J_1 and J_2 interactions. While this has been explored in the hyperkagome lattice where each spin participates in two corner-sharing triangles [19, 20, 21], there has until now been no experimental or theoretical exploration of this more highly connected hyper-hyperkagome lattice where each spin participates in three corner-sharing triangles. Three-dimensional spin liquids are very rare and current examples are confined mostly

to the pyrochlore and hyperkagome lattices, thus our results are highly important because they reveal a new type of three-dimensional lattice capable of supporting spin liquid behaviour.

Methods

Neutron scattering measurements

Powder neutron diffraction was performed on the time-of-flight diffractometer WISH at the ISIS Facility, Didcot, U.K. The sample (weight 13 g) was placed into a copper can and the diffraction patterns were collected at T=2 K and 0.1 K. The powder inelastic neutron scattering data was obtained at the time-of-flight spectrometer LET also located at the ISIS facility. For these measurements the same powder sample (weight 13 g) was placed between two coaxial copper cans to achieve a cylindrical sample shape, and Helium exchange gas was used for better temperature stability. The measurements were performed at T=0.1 K with incident energies: E_i=18.2 meV, 5.64 meV, 2.72 meV, 1.59 meV, 1.04 meV. Single crystal inelastic neutron measurements in the $[h, k, 0]$-plane were obtained at the ThALES triple-axis spectrometer using the flatcone detector at the ILL, Grenoble, France, and also at the MACS triple-axis spectrometer at NIST, Gaithursburg, USA. Wavevector maps at constant energy were measured on ThALES at T=0.05 K while rotating the crystal in 0.5 deg steps with a fixed final energy of E_f=4.06 meV giving an energy resolution 0.097 meV. The wavevector resolution in the plots is 0.05 r.l.u ×0.05 r.l.u. At MACS, the initial energy was set to E_i=4 meV for energy transfer of E=0.75 meV (giving energy resolution of 0.24 meV) and E_i=5 meV for E=1.5 meV and 2 meV (energy resolution 0.35 meV). The wavevector maps were obtained by rotating the crystal with a step size of 1 deg and the data were plotted by rebinning to 0.04 r.l.u×0.04 r.l.u pixels. The maps in $[h, h, l]$ plane were obtained at the LET spectrometer in ISIS at T=0.03 K with incident energies of E_i=26.24 meV, 5.46 meV, 2.29 meV, 1.25 meV, and 0.79 meV. For E_i=5.46 meV this gives an energy resolution of 0.18 meV.

Density functional theory calculations

We determined the parameters of the Heisenberg Hamiltonian in Eq. 1 for $PbCuTe_2O_6$ using density functional theory (DFT) calculations with the all electron full potential local orbital (FPLO) basis [30]. We based our calculations on the structure determined via powder X-ray diffraction by Koteswararao *et al.* [24]. The exchange couplings were extracted by mapping the total energies of many different spin configurations onto the classical energies of the Heisenberg Hamiltonian [31]. Note that this approach is different from the second order perturbation theory estimates using $J=\frac{4t^2}{U}$ for the exchange interactions reported in Ref. [24] which includes only the antiferromagnetic super-exchange contribution based on one

virtual process. In order to increase the number of inequivalent Cu^{2+} ions from one to six and thus to allow for different spin configurations, we lowered the symmetry of the crystal from $P\,4_132$ to $P\,2_1$. We converged the total energies with 6×6×6 **k**-meshes and accounted for the strong electronic correlations using a GGA+U exchange correlation functional [32]. The value of the Hund's rule coupling was fixed at the typical value $J_{\rm H}$=1 eV, and the onsite correlation strength U was varied between 5.5 eV and 8 eV. We determined the most relevant U by using the constraint that the exchange couplings reproduce the experimentally determined Curie-Weiss temperature of $\theta_{\rm CW} = -22$ K [24, 25]. This led to a DFT result for the first four exchange couplings of $PbCuTe_2O_6$ of $J_1 = 1.13$ meV, $J_2 = 1.07$ meV, $J_3 = 0.59$ meV, and $J_4 = 0.12$ meV. The full results are given in the Supplementary Information.

Pseudofermion functional renormalization group calculations

The microscopic spin model proposed by DFT calculations is treated within the PFFRG approach [33, 34], which first reformulates the original spin operators in terms of Abrikosov fermions. The resulting fermionic model is then explored within the well-developed FRG framework [35, 36]. Effectively, the PFFRG method amounts to generating and summing up a large number of fermionic Feynman diagrams, each representing a spin-spin interaction process that contributes to the magnetic susceptibility. In terms of the original spin degrees of freedom, this summation corresponds to a simultaneous expansion in $1/S$ and $1/N$, where S is the spin magnitude and N generalizes symmetry group of the spins from SU(2) to SU(N). The exactness of the PFFRG in the limits $1/S \to 0$ and $1/N \to 0$ ensures that magnetically ordered states (typically obtained at large S) and non-magnetic spin liquids (favoured at large N) can both be faithfully described within the same numerical framework. In principle, the PFFRG treats an infinitely large lattice, however, spin-spin correlations are only taken into account up to a certain distance while longer correlations are put to zero. The computation times of the PFFRG scale quadratically with the correlated volume, which in our calculations comprises 2139 lattice sites (this corresponds to correlations up to a distance of ≈10 nearest-neighbor distances). Likewise, continuous frequency variables (such as the dynamics of the magnetic susceptibility) are approximated by a finite and discrete frequency grid, which leads to a quartic scaling of the computational effort in the number of grid points. In our calculations we use 64 discrete frequencies. The central outcome of the PFFRG approach is the static and momentum-resolved magnetic susceptibility which can be directly related to the experimental neutron scattering cross section through the Kramers-Kronig relation. If a magnetic system develops magnetic order, this manifests in a breakdown of the renormalization group flow, accompanied by distinct peaks in the magnetic susceptibility. An important advantage of the PFFRG is that even in strongly fluctuating non-magnetic phases, short-range spin correlations and their momentum profiles can

be accurately calculated and compared to neutron scattering results. For consistency, the PFFRG spin susceptibility is corrected for the magnetic form factor of the Cu^{2+} ion in the dipole approximation [37].

Classical simulations

For the numerical treatment of spin systems in the classical limit $S \to \infty$ we have employed a spin-S generalization of the PFFRG approach. On a technical level, this requires the introduction of $4S$ fermionic degrees of freedom per lattice site as discussed in Ref. [38]. In the classical limit, the PFFRG equations can be solved analytically to obtain the momentum resolved magnetic susceptibility. It can be shown that the classical wave vector at which the susceptibility is strongly peaked is identical to the one predicted within the Luttinger-Tisza method [39]. The final susceptibility is corrected for the Cu^{2+} magnetic form factor in the dipole approximation.

Data availability

Raw powder neutron diffraction data were measured on the time-of-flight diffractometer WISH at the ISIS facility, Didcot, UK. Raw powder and single crystal inelastic neutron scattering data were measured on the time-of-flight spectrometer LET also at the ISIS facility. Single-crystal inelastic neutron scattering data were also collected on the triple-axis spectrometers ThALES with the flat cone option at the Institut Laue-Langevin, Grenoble, France, and MACS II at the NIST Center for Neutron Research, Gaithersburg, USA. All other raw and derived data used to support the findings of this study are available from the authors on request.

Acknowledgements

We thank K. Siemensmeyer for his help with the susceptibility measurements and D. Voneshen for his help with the inelastic neutron experiments performed on LET at the ISIS facility. S.C., B.L., A.T.M.N.I., and J.R. acknowledge the Helmholtz Gemeinschaft for funding via the Helmholtz Virtual Institute (Project No. HVI-521). Access to MACS was provided by the Center for High Resolution Neutron Scattering, a partnership between the National Institute of Standards and Technology and the National Science Foundation under Agreement No. DMR-1508249. Y.I. and R.T. gratefully acknowledge the Gauss Centre for Supercomputing e.V. for funding this project by providing computing time on the GCS Supercomputer SuperMUC at Leibniz Supercomputing Centre (LRZ). J.R. is supported by the Freie Universität Berlin within the Excellence Initiative of the German Research Foundation.

Author contributions

A.T.M.N.I. made the powder and single crystal samples. S.C. performed or participated in all neutron measurements, and analyzed the data with help from the other authors. J.A.R.-R., R.B., P.S. supported the INS measurements and D.K., P.M. supported the neutron diffraction measurements. B.L. participated in most measurements and directed the experimental aspects of the project. The DFT calculations were performed by H.O.J., Y.I carried out the quantum PFFRG calculations with the help of J.R. and R.T., while J.R performed the classical simulations and directed the theoretical aspects of the project. S.C. and B.L. wrote the manuscript with contributions from all authors.

Additional information

Supplementary information: Included.

Competing financial interests statement: The authors declare no competing financial interests.

References

[1] L. Balents. Spin liquids in frustrated magnets. *Nature*, **464**:199–208, 2010.

[2] B. Lake et al. Quantum criticality and universal scaling of a quantum antiferromagnet. *Nature Materials*, **4**:329–334, 2005.

[3] B. Lake et al. Multispinon Continua at Zero and Finite Temperature in a Near-Ideal Heisenberg Chain. *Phys. Rev. Lett.*, **111**:137205, 2013.

[4] M. Mourigal et al. Fractional spinon excitations in the quantum Heisenberg antiferromagnetic chain. *Nature Physics*, **9**:435441, 2013.

[5] T.-H Han et al. Fractionalized excitations in the spin-liquid state of a kagome-lattice antiferromagnet. *Nature*, **492**:406–410, 2012.

[6] C. Balz et al. Physical realization of a quantum spin liquid based on a novel frustration mechanism. *Nature Physics*, **12**:942–950, 2016.

[7] C. Balz et al. Magnetic Hamiltonian and phase diagram of the quantum spin liquid $Ca_{10}Cr_7O_{28}$. *Phys. Rev. B*, **95**:174414, 2017.

[8] A. Banerjee et al. Proximate Kitaev quantum spin liquid behaviour in a honeycomb magnet. *Nature Materials*, **15**:733–740, 2016.

[9] S.-H. Do et al. Majorana fermions in the Kitaev quantum spin system α-$RuCl_3$. *Nature Physics*, **13**:1079–1084, 2017.

[10] B. Canals and C. Lacroix. Pyrochlore Antiferromagnet: A Three-Dimensional Quantum Spin Liquid. *Phys. Rev. Lett.*, **80**:2933–2936, 1998.

[11] R. Moessner and J. T. Chalker. Properties of a Classical Spin Liquid: The Heisenberg Pyrochlore Antiferromagnet. *Phys. Rev. Lett.*, **80**:2929–2932, 1998.

[12] O. Benton et al. A spin-liquid with pinch-line singularities on the pyrochlore lattice. *Nature Communications*, **7**:329–334, 2016.

[13] L. Savary and L. Balents. Disorder-Induced Quantum Spin Liquid in Spin Ice Pyrochlores. *Phys. Rev. Lett.*, **118**:087203, 2017.

[14] Y. Iqbal et al. Signatures of a gearwheel quantum spin liquid in a spin-$\frac{1}{2}$ pyrochlore molybdate Heisenberg antiferromagnet. *ArXiv e-prints, In press Phys. Rev. Materials (RC)*, 2017.

[15] L. Clark et al. From Spin Glass to Quantum Spin Liquid Ground States in Molybdate Pyrochlores. *Phys. Rev. Lett.*, **113**:117201, 2014.

[16] C. Castelnovo et al. Magnetic monopoles in spin ice. *Nature*, **451**:42–45, 2008.

[17] T. Fennell et al. Magnetic Coulomb Phase in the Spin Ice $Ho_2Ti_2O_7$. *Science*, **326**:415–417, 2009.

[18] D. J. P. Morris et al. Dirac Strings and Magnetic Monopoles in the Spin Ice $Dy_2Ti_2O_7$. *Science*, **326**:411–414, 2009.

[19] J. M. Hopkinson et al. Classical Antiferromagnet on a Hyperkagome Lattice. *Phys. Rev. Lett.*, **99**:037201, 2007.

[20] Y. Zhou et al. $Na_4Ir_3O_8$ as a 3D Spin Liquid with Fermionic Spinons. *Phys. Rev. Lett.*, **101**:197201, 2008.

[21] E. J. Bergholtz et al. Symmetry Breaking on the Three-Dimensional Hyperkagome Lattice of $Na_4Ir_3O_8$. *Phys. Rev. Lett.*, **105**:237202, 2010.

[22] R. Dally et al. Short-Range Correlations in the Magnetic Ground State of $Na_4Ir_3O_8$. *Phys. Rev. Lett.*, **113**:247601, 2014.

[23] P. Schiffer et al. Frustration Induced Spin Freezing in a Site-Ordered Magnet: Gadolinium Gallium Garnet. *Phys. Rev. Lett.*, **74**:2379–2382, 1995.

[24] B. Koteswararao et al. Magnetic properties and heat capacity of the three-dimensional frustrated $PbCuTe_2O_6$. *Physical Review B*, **90**:035141, 2014.

[25] P. Khuntia et al. Spin Liquid State in the 3D Frustrated Antiferromagnet $PbCuTe_2O_6$: NMR and Muon Spin Relaxation Studies. *Physical Review Letters*, **116**:107203, 2016.

[26] L. Wulff and H. Müller-Buschbaum. Planar CuO_4 Polygons and a One-Sided Open $Te^{4+}O_3$ Coordination in $SrCuTe_2O_6$. *Zeitschrift fr Naturforschung B*, **52**:1341 – 1344, 1997.

[27] D. L. Quintero-Castro et al. Magnetic excitations of the gapped quantum spin dimer antiferromagnet $Sr_3Cr_2O_8$. *Phys. Rev. B*, **81**:014415, 2010.

[28] M. Kofu et al. Magnetic-Field Induced Phase Transitions in a Weakly Coupled $s = 1/2$ Quantum Spin Dimer System $Ba_3Cr_2O_8$. *Phys. Rev. Lett.*, **102**:177204, 2009.

[29] C. L. Henley. Power-law spin correlations in pyrochlore antiferromagnets. *Phys. Rev. B*, **71**:014424, 2005.

[30] K. Koepernik and H. Eschrig. Full-potential nonorthogonal local-orbital minimum-basis band-structure scheme. *Phys. Rev. B*, **59**:1743–1757, 1999.

[31] D. Guterding et al. Reduction of magnetic interlayer coupling in barlowite through isoelectronic substitution. *Phys. Rev. B*, **94**:125136, 2016.

[32] A. I. Liechtenstein et al. Density-functional theory and strong interactions: Orbital ordering in Mott-Hubbard insulators. *Phys. Rev. B*, **52**:R5467–R5470, 1995.

[33] J. Reuther and P. Wölfle. J_1-J_2 frustrated two-dimensional Heisenberg model: Random phase approximation and functional renormalization group. *Phys. Rev. B*, **81**:144410, 2010.

[34] Y. Iqbal et al. Functional renormalization group for three-dimensional quantum magnetism. *Phys. Rev. B*, **94**:140408, 2016.

[35] J. Polchinski. Renormalization and effective lagrangians. *Nuclear Physics B*, **231**:269 – 295, 1984.

[36] J. Reuther and R. Thomale. Functional renormalization group for the anisotropic triangular antiferromagnet. *Phys. Rev. B*, **83**:024402, 2011.

[37] P. J. Brown. *Magnetic Form Factors*, pages 454–461. Springer Netherlands, Dordrecht, 2004.

[38] M. L. Baez and J. Reuther. Numerical treatment of spin systems with unrestricted spin length S: A functional renormalization group study. *Phys. Rev. B*, **96**:045144, 2017.

[39] J. M. Luttinger and L. Tisza. Theory of Dipole Interaction in Crystals. *Phys. Rev.*, **70**:954–964, 1946.

[40] J. P. Perdew et al. Generalized Gradient Approximation Made Simple. *Phys. Rev. Lett.*, **77**:3865–3868, 1996.

Figure:1

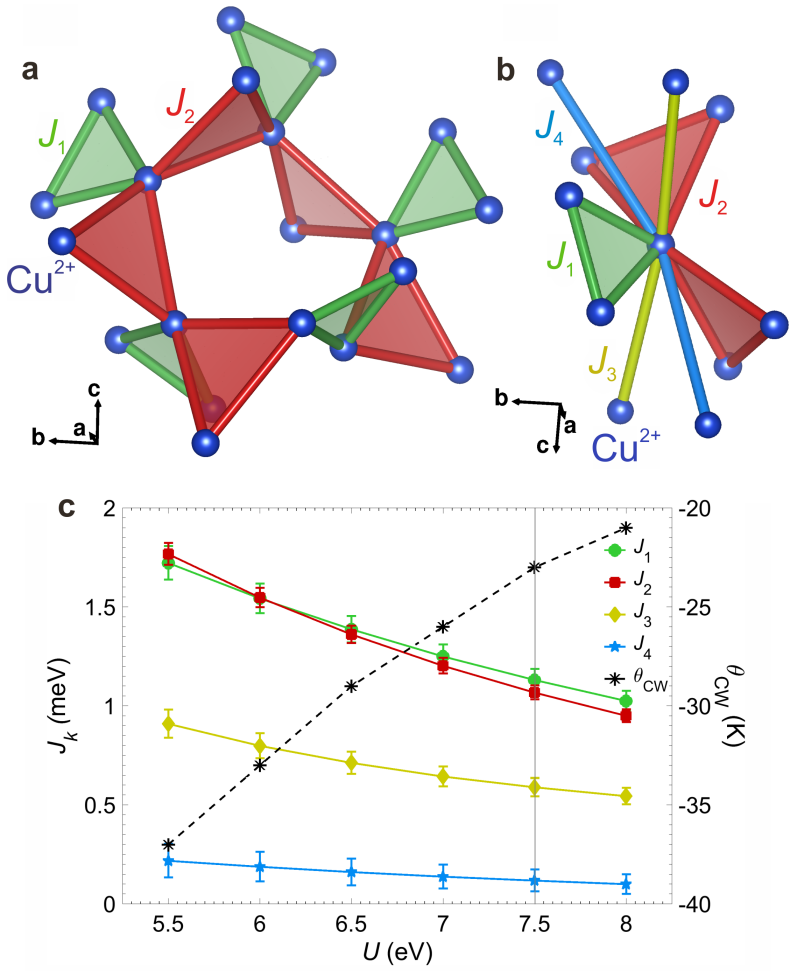

Figure 1: **The magnetic interactions and Hamiltonian of $PbCuTe_2O_6$. a** Structure of $PbCuTe_2O_6$ showing only the magnetic $S=\frac{1}{2}$ Cu^{2+} ions and the 1st and 2nd nearest-neighbor interactions J_1 and J_2 respectively. J_1 forms isolated equilateral triangles whereas J_2 leads to a three-dimensional network of corner-sharing triangles also known as the *hyperkagome* lattice. The 3rd and 4th neighbour couplings J_3 and J_4, respectively, are also included in **b** and couple the Cu^{2+} ions into chains. The chains formed by J_3 run parallel to the cubic **a**, **b**, **c** axes while the chains due to J_4 follow the body diagonals. $PbCuTe_2O_6$ crystallizes in *cubic* symmetry with *space group* $P\,4_132$ and the Cu^{2+} ions occupy a single Wyckoff site [26]. The graph in **c** shows the strengths of the four nearest neighbour interactions as a function of Cu^{2+} onsite interaction U calculated by density functional theory (coloured symbols, left hand axis). These calculations were performed with the full potential local orbital basis (FPLO) set [30], and the generalized gradient approximation functional [40]; the coupling constants were then determined by fitting to the Hamiltonian in Eq. 1. The error bars indicate statistical errors of the fit. The Curie-Weiss temperature was calculated for each set of exchange constants using $\theta_{\rm CW} = -\frac{S(S+1)}{3k_b}\sum_{k=1}^{4} z_k J_k$ (for single-counting of bonds) where z_k is the coordination number of the $J_k^{\rm th}$ interaction (black stars, right hand axis). All the interactions are antiferromagnetic. J_1 and J_2 are approximately equal, and much stronger than J_3 and J_4. Together, J_1 and J_2 result in the hyper-hyperkagome lattice where each magnetic ion participates in three corner-sharing triangles (compared to two triangles in the hyperkagome latice). These results differ significantly from the ratio of couplings, $J_1{:}J_2{:}J_3{=}0.54{:}1{:}0.77$ estimated previously by second-order perturbation theory ($J{=}\frac{4t^2}{U}$, $t \equiv$ hopping parameter) that calculates the couplings based on a selected virtual process unlike DFT which includes ferromagnetic and antiferromagnetic contributions to the exchange interactions. [24]. Those results suggested that J_2 was the strongest interaction, being twice the strength of J_1, while J_3 was also large, and J_4 was not considered.

Figure:2

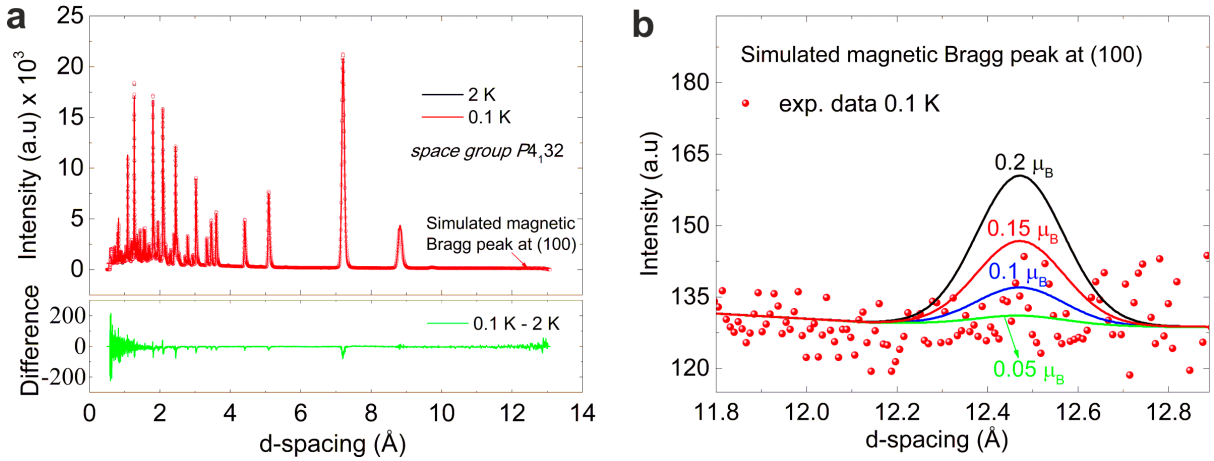

Figure 2: **Powder neutron diffraction patterns of $PbCuTe_2O_6$. a** Measured at 0.1 K and 2 K using the WISH high-flux diffractometer and plotted as a function of d-spacing. Both patterns are refined in the established cubic space group, $P\,4_132$ [26] where the lattice constant at 0.1 K is $12.4454(3)$ Å. The difference between the patterns at these two temperatures is plotted below in green and clearly shows that no magnetic Bragg peaks appear at the base temperature. **b** Assuming a magnetic structure compatible with the long range magnetic order found in $SrCuTe_2O_6$, a magnetic Bragg peak is estimated at the $(1,0,0)$ reflection (12.4454 Å in d-spacing). The expected Bragg peak amplitude is shown for different values of ordered moment per Cu^{2+} ion by the curves. Clearly, if present, the maximum ordered moment can be no greater than 0.05 μ_B.

Figure:3

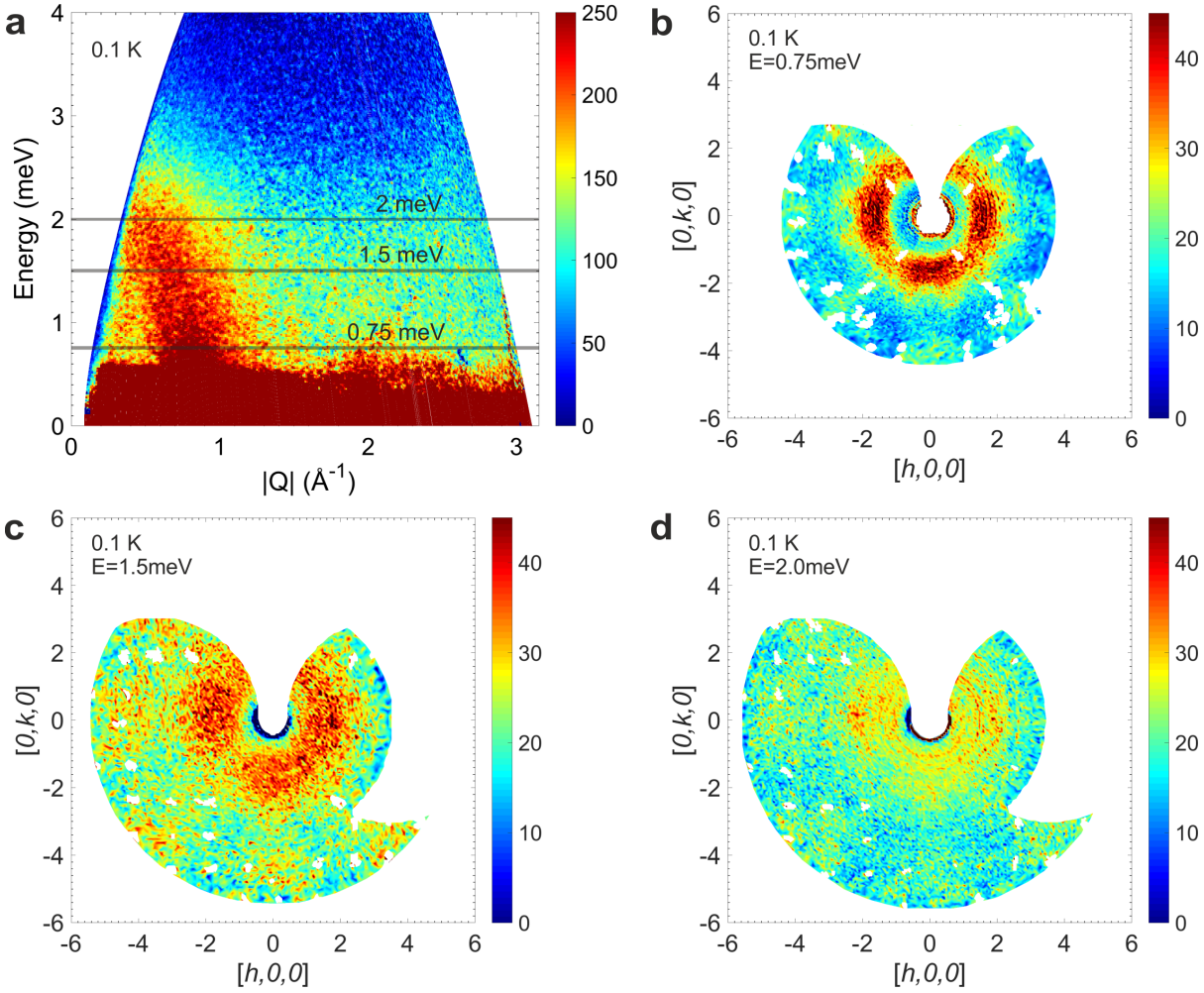

Figure 3: **Magnetic inelastic neutron scattering data of $PbCuTe_2O_6$ measured at temperatures of $\mathbf{T < 0.1\ K}$.** **a** Powder spectrum obtained using the time-of-flight spectrometer LET, with an incident energy of 5.76 meV. This plot clearly shows the presence of a diffuse, dispersionless continuum of magnetic excitations extending up to $E \approx 3$ meV. **b-d** Single crystal spectra measured in the MACS spectrometer in the $[h, k, 0]$-plane at constant energy transfers of E$= 0.75$ meV, 1.5 meV, and 2 meV respectively. Non-magnetic features such as phonons and Bragg peak tails have been removed from the spectrum. The color map at 0.75 meV reveals a broad, diffuse ring-like feature at $|Q| \approx 0.8$ Å^{-1} whose intensity modulates with maxima at $(1.69, \pm 0.3, 0)$, and equivalent positions. Similar features are present at higher energies with reduced intensity. The uncertainties in figures **b-d** correspond to one standard deviation.

Figure:4

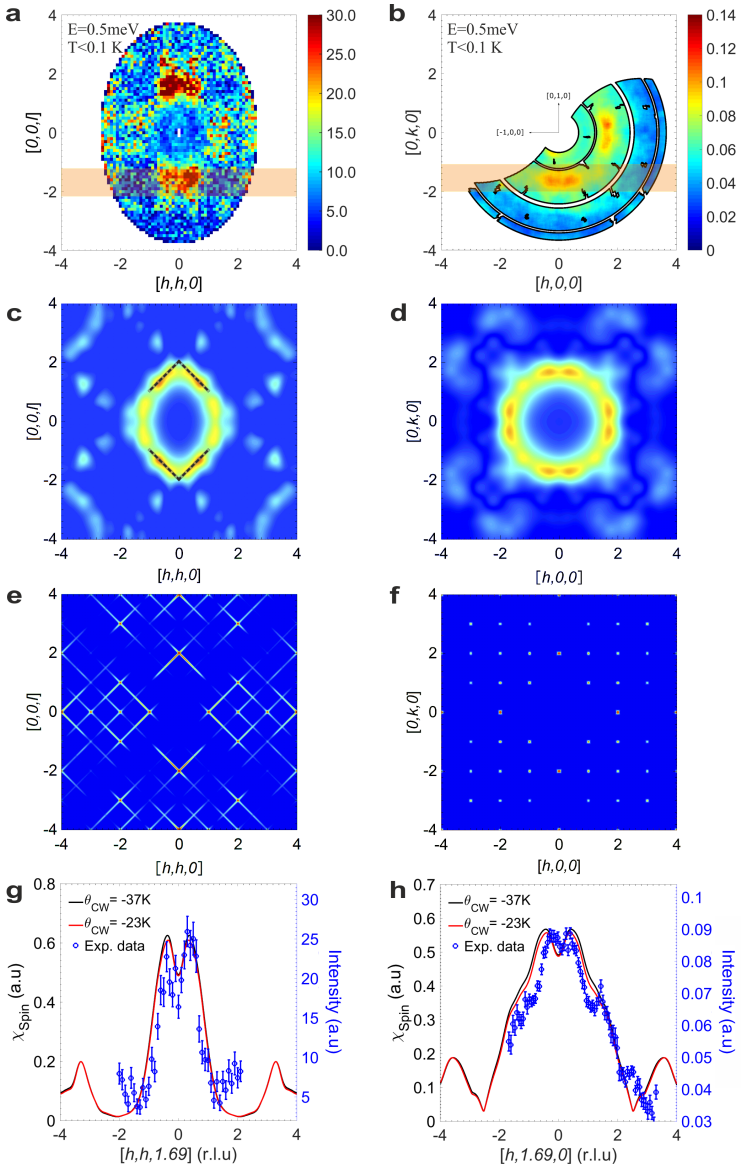

Figure 4: **The low energy magnetic excitation spectrum of $PbCuTe_2O_6$ compared to theory.** The color maps in **a** and **b** show the excitations measured at energy transfer E=0.5 meV and temperature $T < 0.1$ K in the $[h, h, l]$- and $[h, k, 0]$-planes respectively. The $[h, h, l]$-map was measured using the LET spectrometer with an incident energy of $E_i = 5.46$ meV. The data has been integrated over energy transfer $0.4 \leqslant E \leqslant 0.6$ meV, and out-of-plane wave-vector transfer $-0.1 \leqslant [h, -h, 0] \leqslant 0.1$ r.l.u. The $[h, k, 0]$ spectrum was measured on the ThALES spectrometer with an energy resolution of 0.097 meV. **c** and **d** Static (real valued) spin susceptibility calculated using the pseudo-fermion functional renormalization group (PFFRG) method in the quantum limit (S=1/2) for J_1=1.13 meV, J_2=1.07 meV, J_3=0.59 meV, and J_4=0.12 meV (corresponding to a Curie-Weiss temperature $\theta_{\rm CW} = -23$ K). The dashed black lines indicate the positions of strong scattering in the classical J_1-J_2-only model [see **e** and **f**]. **e** and **f** Corresponding classical PFFRG results obtained in the limit of large spin magnitude for a model with only J_1 and J_2 couplings of equal strength. **g** and **h** The experimental and theoretical magnetic intensity as a function of wave-vector transfer along $[h, h, -1.69]$ and $[h, -1.69, 0]$ respectively. The data points (blue circles) were measured at an energy transfer E=0.5 meV and temperature T<0.1 K and were obtained by integrating the data shown in **a** and **b** over the respective shaded regions. The solid lines show the theoretical intensity obtained by performing the same integration through the theoretical simulations. The theoretical intensity distribution is also shown for another set of exchange interactions represented by their corresponding Curie-Weiss temperature $\theta_{\rm CW} = -37$ K (see Figure. 1c). The calculations in **c** to **h** are corrected for the Cu^{2+} form factor and the error bars in **g** and **h** represent statistical errors.

Supplementary Information: A quantum spin liquid based on a new three-dimensional lattice

DC susceptibility

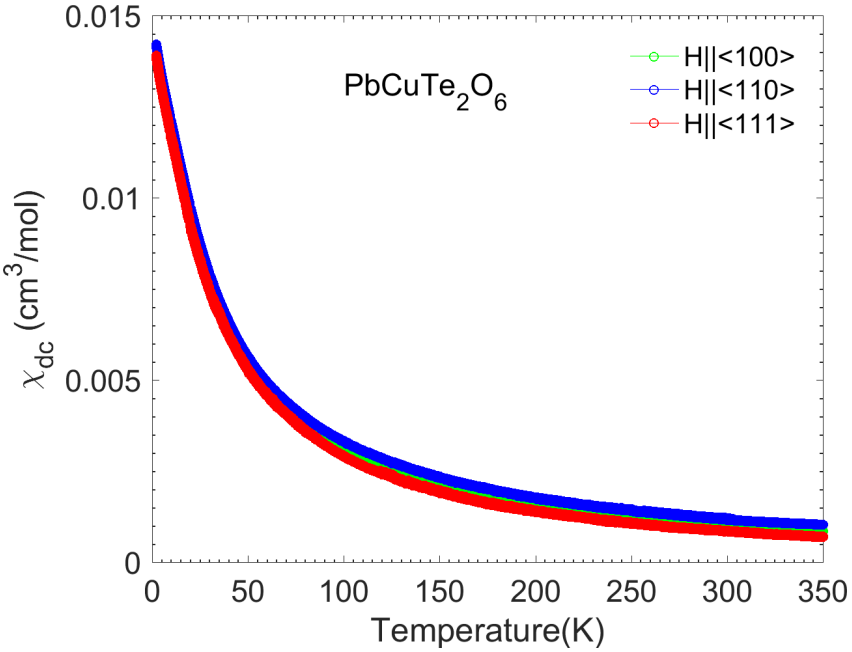

Figure. S 1: **The static magnetic susceptibility measured on a single crystal of $PbCuTe_2O_6$.** With magnetic field applied parallel to the three inequivalent directions of the cubic system, $[1,0,0]$, $[1,1,0]$ and $[1,1,1]$. The sample is cooled in zero field and the susceptibility is measured as a function of temperature in a constant field of H= 1T. The plot reveals that the susceptibility is nearly the same for all the directions indicating that the system can be considered magnetically isotropic.

In order to verify the isotropic nature of the Cu^{2+} moments in $PbCuTe_2O_6$, static (DC) susceptibility measurements on single crystal samples have been compared for three inequivalent magnetic field directions within the cubic system. For this purpose, the zero-field cooled moment was measured under a H= 1 T field applied parallel to the $[1,0,0]$, $[1,1,0]$ and $[1,1,1]$ crystallographic directions for temperatures in the range T=2 K to 350 K. Figure S 1 shows that the susceptibility displays no indication of any phase transitions down to 2 K. Furthermore the susceptibility is almost completely independent of the field direction. Therefore, we can conclude that the Cu^{2+} spin-$\frac{1}{2}$ moments in $PbCuTe_2O_6$ are isotropic in nature making this compound a Heisenberg spin liquid.

Further inelastic neutron scattering measurements

The powder inelastic neutron scattering measurements of $PbCuTe_2O_6$ reveal broad continuua of magnetic excitations. These form a dispersionless band centered around the wavevector $|Q| \sim 0.8\mathring{A}^{-1}$ and extending up to 3 meV (see Figure 3a of the main article). The presence of diffuse scattering is also

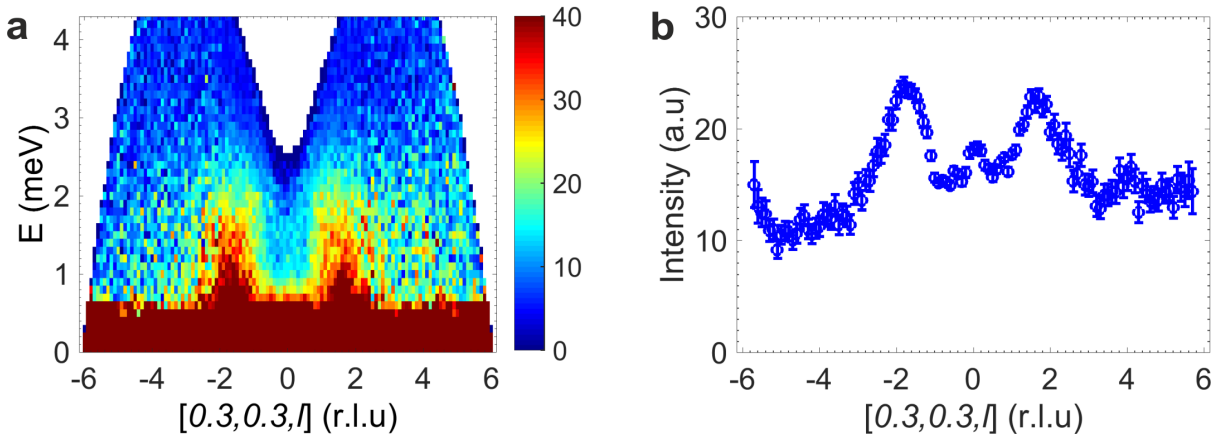

Figure. S 2: **Single crystal excitation spectrum of $PbCuTe_2O_6$ single crystal.** **a** Measured at temperature $T = 0.1$ K on the LET spectrometer at the ISIS facility and plotted as a function of energy and wavevector along the $[0.3, 0.3, l]$ direction. The intensity is obtained by integrating the scattering over $0 < h < 0.6$ and $0 < k < 0.6$ to include the peak maxima on the diffuse scattering sphere as seen in Figure 3b-d and Figure 4a-b of the main article. **b** displays the same data integrated over the energy transfers 0.6 meV<E<3 meV. This plot clearly shows the maxima at $[0.3, 0.3, \sim \pm 1.69]$ (r.l.u).

confirmed by the single crystal neutron data as shown in Figure 3b-d and Figure 4a-b of the main article. These constant energy transfer maps reveal a diffuse sphere of intensity with double maxima at $[0.3, 0.3, \pm 1.69]$ and equivalent positions. The plot in Figure S 2a shows the continuua of excitations along the $[0.3, 0.3, l]$ direction. Strong scattering intensity is observed at $[0.3, 0.3, \pm 1.69]$ and weak continuua are also present at the higher wavevector $[0.3, 0.3, \pm 3.8]$. These continuua appear as small peaks when the data is integrated over energy transfers of $0.8 < E < 3$ meV as shown in Figure S 2b.

Comment on previous Density functional theory calculations in Ref. [S1]

The energy mapping method applied in our density functional theory calculations employs fully charge self-consistent solutions for different spin configurations, therefore it includes at the density functional theory level the exchange contributions to arbitrary order. It is clear that this approach yields different and usually more reliable estimates than the second-order perturbation theory formula $J = \frac{4t^2}{U}$ used previously [S1] which expresses only the antiferromagnetic superexchange contribution based on one virtual process. The latter approximation leaves out a large number of other exchange processes both from higher orders of perturbation theory as well as ferromagnetic contributions. The results from our DFT calculations yield interactions up to 4^{th} nearest neighbour with a ratio of J_1:J_2:J_3:J_4=1.06:1:0.55:0.11 for the Curie-Weiss temperature of $\theta_{CW} = -23$ K. In contrast, the previous method finds only the first three neighbours to be relevant and the ratio of couplings is J_1:J_2:J_3=0.54:1:0.77. The difference between the two methods is evident in the spin susceptibility maps calculated using the PFFRG method based on the Hamiltonian from these two sets of couplings as shown in Figure S 3. Although the static spin

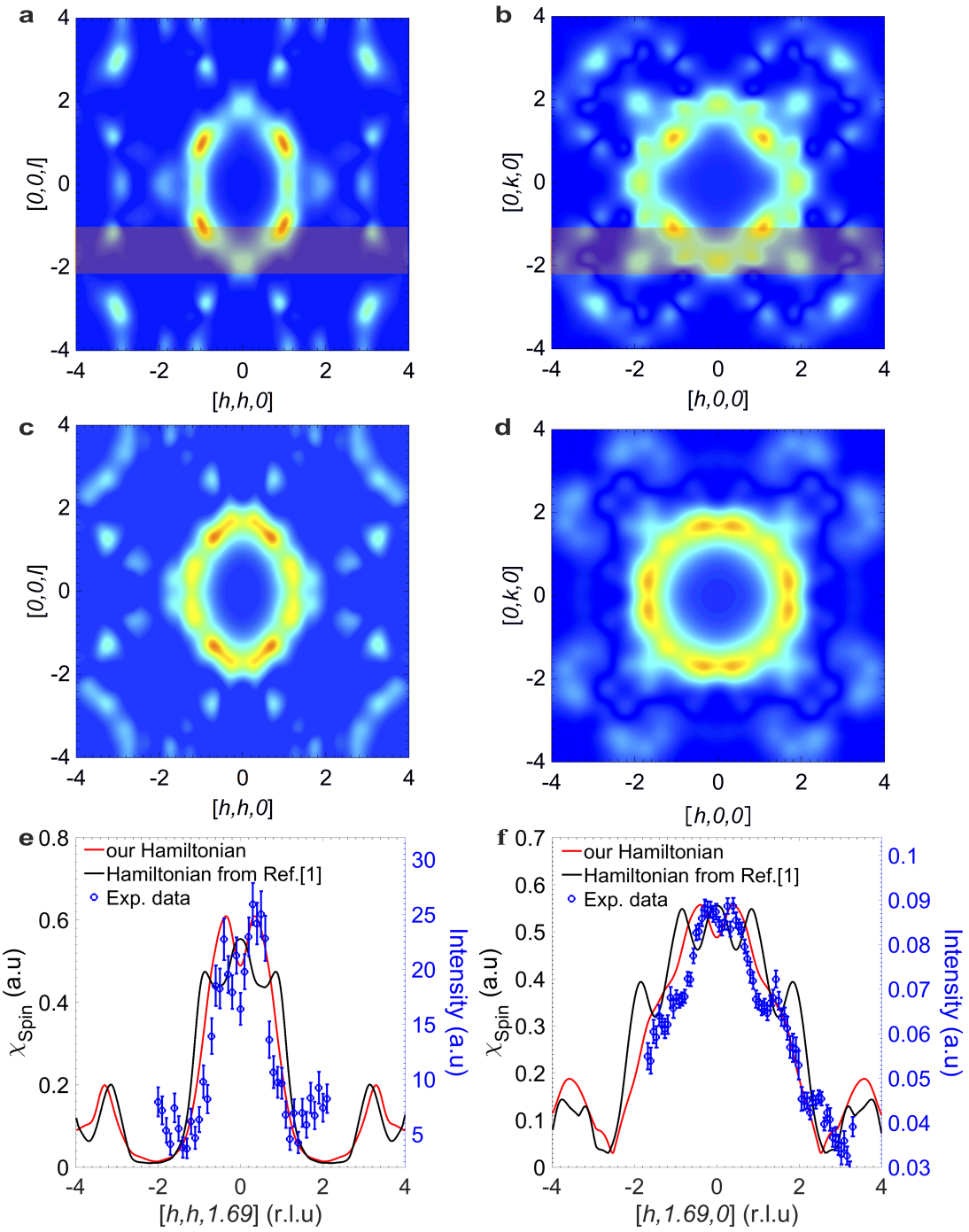

Figure. S 3: **The static spin susceptibility profiles calculated using the PFFRG method.** From the Hamiltonian produced by: **a**-**b** second-order perturbation theory that expresses only the antiferromagnetic superexchange contribution based on one virtual process (Ref. [S1]): and **c**-**d** the current work that employs the full potential local orbital basis set [S2] and the generalized gradient approximation functional [S3]. The former results produce a sharper diffuse ring in $[h, h, l]$ plane with maxima at (1,1,1) and a diamond shaped profile in the $[h, k, 0]$ plane which do not agree with the experimental data. The latter results however show striking similarity with our neutron scattering maps. **e**-**f** Comparison between cuts through the experimental data and the expected magnetic intensity calculated for the two Hamiltonians using PFFRG. The data points were obtained by integrating the experimental data shown in figure 4 **a** and **b** of the main paper, over the respective shaded regions indicated in those figures. The same integration was performed over the calculations (see shaded region in **a** and **b**). As is clearly evident, our Hamiltonian gives much better agreement with the data than the previous Hamiltonian.

susceptibility based on the Hamiltonian from the perturbation theory method [S1] also produces a ring at $\sim 0.8\ \mathring{A}^{-1}$, as shown in Figure S 3a, the maxima on the ring appear at $(1,1,1)$ and equivalent positions in the $[h,h,l]$-plane. This is clearly different from the experimental results where the diffuse ring is broad and the maxima are at positions such as $(0.3, 0.3, \pm 1.69)$ as nicely reproduced by the Hamiltonian from our DFT calculations (see Figure S 3c). The discrepancy of the previous Hamiltonian is even clearer in the $[h,k,0]$ plane (compare Figure S 3b & d) where the double peak at $(\pm 1.69, \pm 0.3, 0)$ is missing. Figure 3e & f show cuts through the data and the calculated spin susceptibility of the two Hamiltonians. The agreement between our Hamiltonian and the data is clearly much better than that of the previous Hamiltonian [S1].

Ground state properties of classical Heisenberg models on the hyperkagome lattice

As discussed in the main text, the origin of the spin fluctuations in $PbCuTe_2O_6$ can be explained within a classical Heisenberg model that includes only the triangular J_1 and hyperkagome J_2 interactions even though this material also features additional J_3 and J_4 couplings. In particular, the streaks in the momentum resolved classical susceptibility of the J_1-J_2 model resemble the PFFRG quantum calculation of the full model, as shown for the $[h,h,l]$ plane in Figure 4e. The susceptibility in the $[h,k,0]$ plane (Figure 4f) shows points of strong intensity since this plane cuts through the streaks.

This correlation profile can be compared with a classical Heisenberg model with J_2 hyperkagome interactions only, as it has previously been studied in Ref. [S4]. The ground state of this model is macroscopically degenerate, i.e. for a system consisting of $L \times L \times L$ unit cells, the dimension of the degenerate manifold scales exponentially as $V{=}L^3$. As a consequence, the spin structure factor shows extended regions of strong intensity which fill a volume in momentum space, see Figure 2 in Ref. [S4]. Furthermore, in close similarity to classical pyrochlore systems, where an "ce rule" for each tetrahedron/triangle imposes a constraint on the local spin orientation, the structure factor exhibits pinch points.

When triangle J_1 interactions are added, further constraints are imposed on the possible ground states, which reduce the dimensionality of the degenerate ground state manifold. Particularly, it can be shown that the number of degenerate states becomes subextensive, i.e. it scales exponentially in the linear system size L [S5]. As a consequence, the regions of strong intensity in the structure factor shrink down to lines parallel to the $[1,1,1]$ (and symmetry related) directions. Interestingly, the susceptibility in Fig. 4e still shows remainders of the pinch points such as the point $[0,0,2]$ where streaks of high intensity cross.

It is important to emphasize that even though the classical J_1-J_2 Heisenberg model only exhibits a subextensive ground state degeneracy, there is still a macroscopic number of low-energy states through which the system can fluctuate when quantum fluctuations are considered [S5]. This still remains true when the weaker J_3 and J_4 interactions are added. While this further reduces the degeneracy to a finite number of states, the full manifold of the classical J_1-J_2 Heisenberg model still remains energetically nearby.

References

[S1] B. Koteswararao et al. Magnetic properties and heat capacity of the three-dimensional frustrated $PbCuTe_2O_6$. *Physical Review B*, **90**:035141, 2014.

[S2] K. Koepernik and H. Eschrig. Full-potential nonorthogonal local-orbital minimum-basis band-structure scheme. *Phys. Rev. B*, **59**:1743–1757, 1999.

[S3] J. P. Perdew et al. Generalized Gradient Approximation Made Simple. *Phys. Rev. Lett.*, **77**:3865–3868, 1996.

[S4] J. M. Hopkinson et al. Classical Antiferromagnet on a Hyperkagome Lattice. *Phys. Rev. Lett.*, **99**:037201, 2007.

[S5] Y. Iqbal et al. *in preparation.*